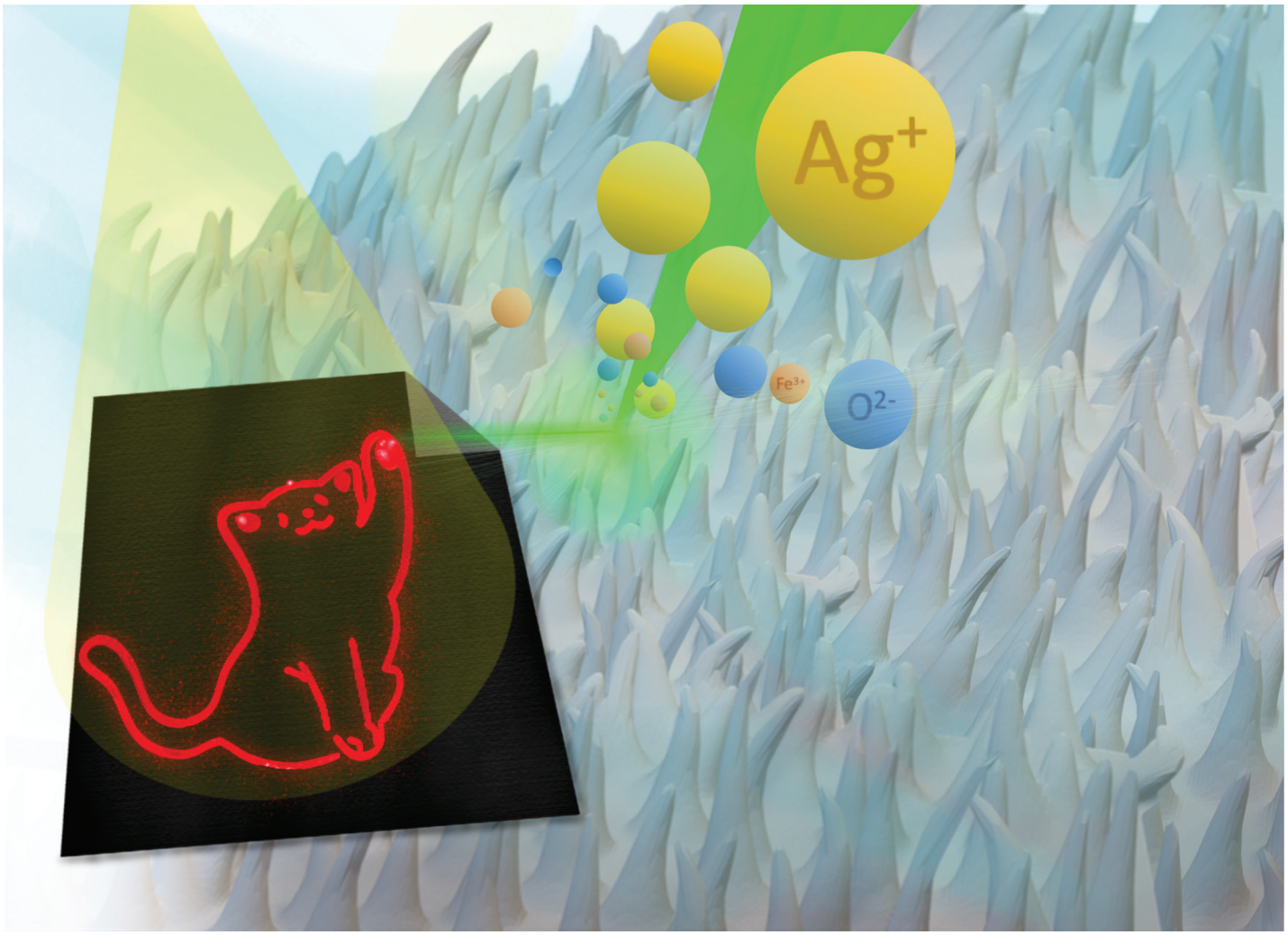

Showcasing research from Professor Chorng Haur Sow's Nanomaterials Research Lab, National University of Singapore, Singapore.

Laser-initiated site-selective formation of fluorescing silver–iron oxide nanocomposites for electron detection

A site-selective and facile means of forming silver–iron oxide nanocomposites is achieved by directing a continuous wave laser at iron oxide nanoflake surface while submerging the flakes in a silver nitrate solution. The nanocomposite's size and properties can be tuned by varying the lasering parameters, such as speed and laser power density. Uniquely, these nanocomposite particles exhibit bright red fluorescence under yellow light excitation, allowing optical determination of composite formation. This composite also emits stronger fluorescence after electron interaction, allowing it to serve as an electron irradiation detector with optical feedback.

Image reproduced by permission of Yue Yin, Chorng Haur Sow and Sharon Xiaodai Lim from *Nanoscale*, 2025, **17**, 20935.

As featured in:

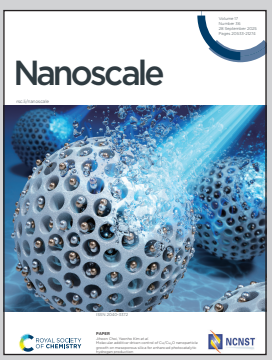

See Yue Yin, Chorng Haur Sow, Sharon Xiaodai Lim *et al.*, *Nanoscale*, 2025, **17**, 20935.

ROYAL SOCIETY OF CHEMISTRY

rsc.li/nanoscale

Registered charity number: 207890

Nanoscale

ROYAL SOCIETY OF CHEMISTRY

PAPER

View Article Online
View Journal | View Issue

Cite this: *Nanoscale*, 2025, **17**, 20935

Laser-initiated site-selective formation of fluorescing silver–iron oxide nanocomposites for electron detection

Yue Yin,[a] Aseera Jannath,[a] Zheng Zhang,[b] Chorng Haur Sow[c] and Sharon Xiaodai Lim *[c]

Received 30th May 2025,
Accepted 11th August 2025

DOI: 10.1039/d5nr02284c

rsc.li/nanoscale

There has been ongoing interest in the fabrication of silver–iron oxide composite nanostructures due to their effectiveness in antimicrobial, catalytic, and sensing applications. However, traditional processes involve multiple steps and harsh conditions, making them time-consuming and energy-intensive. A focused laser beam is used as an alternative tool to fabricate fluorescent silver–iron oxide composite nanostructures. The rapid thermal annealing and quenching process results in uniformly distributed particles that form site-selectively in the laser-irradiated regions. When performing without demanding conditions or additives, this process is more precise, energy-efficient, and cost-effective compared to traditional methods. The presence of silver within the composite enhances the intrinsic fluorescence of Fe_3O_4 by more than 10 times through surface plasmon resonance effects. This exclusive trait turns the composite into an effective micro-beta particle detector with *in situ* optical feedback. This work provides a glimpse into the benefits of developing alternative synthesis processes as a means to uncover new applications.

1 Introduction

The synthesis of silver–iron oxide nanostructures has attracted continued interest due to its effectiveness in biomedical,[1] environmental remediation,[2] catalysis,[3] electronic[4] and sensing applications. As antimicrobial agents, they are particularly effective due to the synergistic effects of silver and its iron oxide substrate.[5] They are also used in the catalytic degradation of water pollutants[2,3,6] and to detect CO, NO, and volatile organic compounds (VOCs).[5]

Many methods have been explored over the years for the synthesis of silver–iron oxide nanocomposites. Traditional methods include the sol–gel method,[5] the hydrothermal method[7] and the co-precipitation method.[2] More recently, much effort has been devoted to the development of green synthesis methods using biological extracts.[8–11] The sol–gel method offers the benefit of good control over particle size and homogeneity. However, it can be costly due to its requirements of specific precursors, controlled environments, and stabilising agents to be added. Furthermore, such processes are energy-intensive due to the drying and calcination processes conducted at high temperatures. The hydrothermal method also provides good control over particle morphology and size, but it also suffers from high energy consumption due to the need to maintain elevated temperatures and pressures. Co-precipitation can be cheap and scalable, but offers limited control over size and morphology. The process of co-precipitation also requires the addition of chemical surfactants and stabilisers. While green synthesis methods improve traditional precipitation methods by substituting more eco-friendly biological extracts for chemical reducing agents and stabilisers, the process suffers from the same limitations regarding inhomogeneous size and morphology.

This work attempts to address the above limitations by exploring a different avenue for synthesising silver–iron oxide nanocomposites. A focused laser beam initiates the site-selective photothermal reduction of aqueous silver ions (Ag^+). The strong but localised heating allows silver–iron oxide nanocomposites to be formed evenly under ambient conditions without surfactants or stabilising additives. As a result, the process is a cost and energy-efficient alternative to traditional methods. Relatively good control over particle size and morphology is also achieved. Furthermore, this method has the distinctive feature of site-selectivity, that is, the formation of a nanocomposite is controlled within the site of the laser treat-

[a]*Raffles Institution, 1 Raffles Institution Lane, Singapore 575954, Singapore*
[b]*Institute of Materials Research and Engineering (IMRE), Agency for Science, Technology and Research (A*STAR), 2 Fusionopolis Way, Innovis #08-03, Singapore 138634, Singapore*
[c]*Department of Physics, National University of Singapore, 2 Science Drive 3, Singapore 117542, Singapore. E-mail: phylimx@nus.edu.sg; Tel: (+65) 6516 1161*

ment only. This facilitates the precision engineering of highly specific arrangements of the nanostructure to micrometre precision, and as we enter an age of micro- and nano-sized devices and lab-on-a-chip applications, the ability to conduct precise directed assembly of various micro- and nano-structures could be increasingly valuable.[12]

Uniquely, the silver–iron oxide nanocomposite formed emits strong red fluorescence under yellow excitation. This fluorescing phenomenon is due to Ag amplifying the intrinsic red fluorescence of crystalline Fe_3O_4 by more than 10 times. The fluorescence property thus serves as a simple and reliable means of determining successful nanocomposite formation without requiring more expensive characterisation. While characterising the composite material, the fabricated nanocomposite reacts to electron irradiation with an increase in its fluorescence intensity after being exposed to an electron beam. Through determining the composition of irradiated and non-irradiated samples, as well as an *in situ* observation of the nanostructure's changes during electron irradiation at the atomic level using TEM, the mechanism of this change is identified to be due to the solid-state reduction of silver oxides into silver by electron bombardment. In other words, the fluorescence from the silver–iron oxide nanocomposite can respond to the changes in the oxidation state of silver. This unique property opens the possibility of new applications for a well-known nanocomposite: (i) a micro-beta particle detector with real-time optical feedback or (ii) a pathway for developing cheap, non-destructive optical probing capable of monitoring the degradation of silver catalysts and plasmonic devices. Thus, this work also highlights the benefits of developing alternative synthesis processes for traditional materials, as it allows us to uncover unique features and applications.

2 Experiments

2.1 Materials and methods

2.1.1 Formation of the iron oxide nanoflake substrate. Iron oxide nanoflakes were synthesised using the hotplate method.[13] Iron foil (Sigma-Aldrich, 0.025 mm thick) was polished to remove surface oxidation and cleaned with isopropanol. It was then placed directly on a hotplate (Thermofisher) and heated in air at 400 °C for varying durations (1, 3, 6, 10, and 20 hours).

2.1.2 Laser-initiated photo-reduction of silver on iron oxide nanoflakes. Following the successful growth of the iron oxide nanoflakes, a focused laser beam (FLB) setup was used to initiate the formation of the silver–iron oxide nanocomposite. A green diode laser (532 nm) was used. The laser beam was first passed through a neutral density filter, which facilitates fine-tuning of the beam intensity, and then reflected into an optical microscope using two plane mirrors. A dichroic mirror then redirects the laser to be focused *via* a 100× objective lens into a spot of diameter 1.5 μm. The sample was affixed to a glass slide using a small piece of double-sided tape and then placed on a MICOS *X–Y* stage controlled by Microsoft Visual Basic software.

A thin piece of 1 : 12 base to the curing agent (w : w) polydimethylsiloxane (PDMS) polymer (Sylgard) acts as a well to ensure the silver nitrate solution remains in contact with the underlying substrate. To do so, a piece of PDMS with a rectangular piece cut out from its centre was placed on top of the iron oxide nanoflake substrate. A micro-pipette was used to fill this well with a 0.1 M concentration of silver nitrate solution. Lastly, a glass cover slip was placed over the PDMS well to eliminate the possibility of laser attenuation due to meniscus formation. Laser treatment of the iron oxide substrate in an aqueous silver nitrate environment was achieved by focusing the laser beam on the substrate surface within the PDMS well.

2.1.3 Further characterisation. Further characterisation studies were carried out using the following techniques: fluorescence microscopy (FM, Olympus BX51) under bright-field (BF) light and yellow (530–580 nm) wavelength light excitation; Raman spectroscopy and photoluminescence (PL) spectroscopy (Renishaw inVia Qontor with a 532 nm laser); transmission electron microscopy (TEM, JEOL 2010F); scanning electron microscopy (SEM, JEOL JSM6700-F) and energy dispersive X-ray spectroscopy (EDX, Oxford Instruments X-MaxN 150); X-ray photoelectron spectroscopy (XPS) analyses, which were carried out using a Thermo Fisher Scientific Theta Probe XPS with monochromatic Al K alpha X-rays (1486.7 eV) with charge correction for binding energy based on the C 1s peak from adventitious carbon at 285.0 eV; and X-ray diffraction (XRD) analyses, in which data were collected using a Bruker D8 Advance Powder XRD with Cu K alpha radiation.

3 Results and discussion

3.1 Formation of Fe_2O_3/Fe_3O_4 nanoflakes

Fe_2O_3/Fe_3O_4 nanoflakes were grown *via* the solid–liquid–solid growth mechanism.[13] In essence, when the temperature of the hotplate is sufficiently high, the surface layer of the iron foil begins to melt, forming a liquid medium. Subsequently, the liquid medium adsorbs the oxygen in air and oxidised to iron(II, III) oxide (Fe_3O_4). Fe_3O_4 oxidises readily to Fe_2O_3 at an elevated temperature and precipitates out of the liquid medium after supersaturation to form the flake structure, exposing the next layer of iron atoms. This growth process then repeats continually with subsequent layers until all the iron foil is converted to oxide or until cooling down, whichever takes place first.

Since the iron foil used in this study is very small and thin, the entire piece heats up to 400 °C rapidly and the entire growth process (melting, adsorption of atmospheric oxygen, oxidation to Fe_3O_4, and oxidation to Fe_2O_3) occurs at thermal equilibrium. From the time-dependent XRD and Raman analysis of the iron foil obtained at different heating durations (Fig. S1), it is observed that the resulting iron oxide nanoflakes comprise both Fe_2O_3 and Fe_3O_4, with the majority Fe_2O_3 on the surface. The suggested growth mechanism of the Fe_2O_3/Fe_3O_4 iron oxide nanoflakes, as achieved in this study, is detailed in the SI.

SEM images of the nanoflakes after varying heating durations are shown in Fig. 1(a), with the corresponding optical images

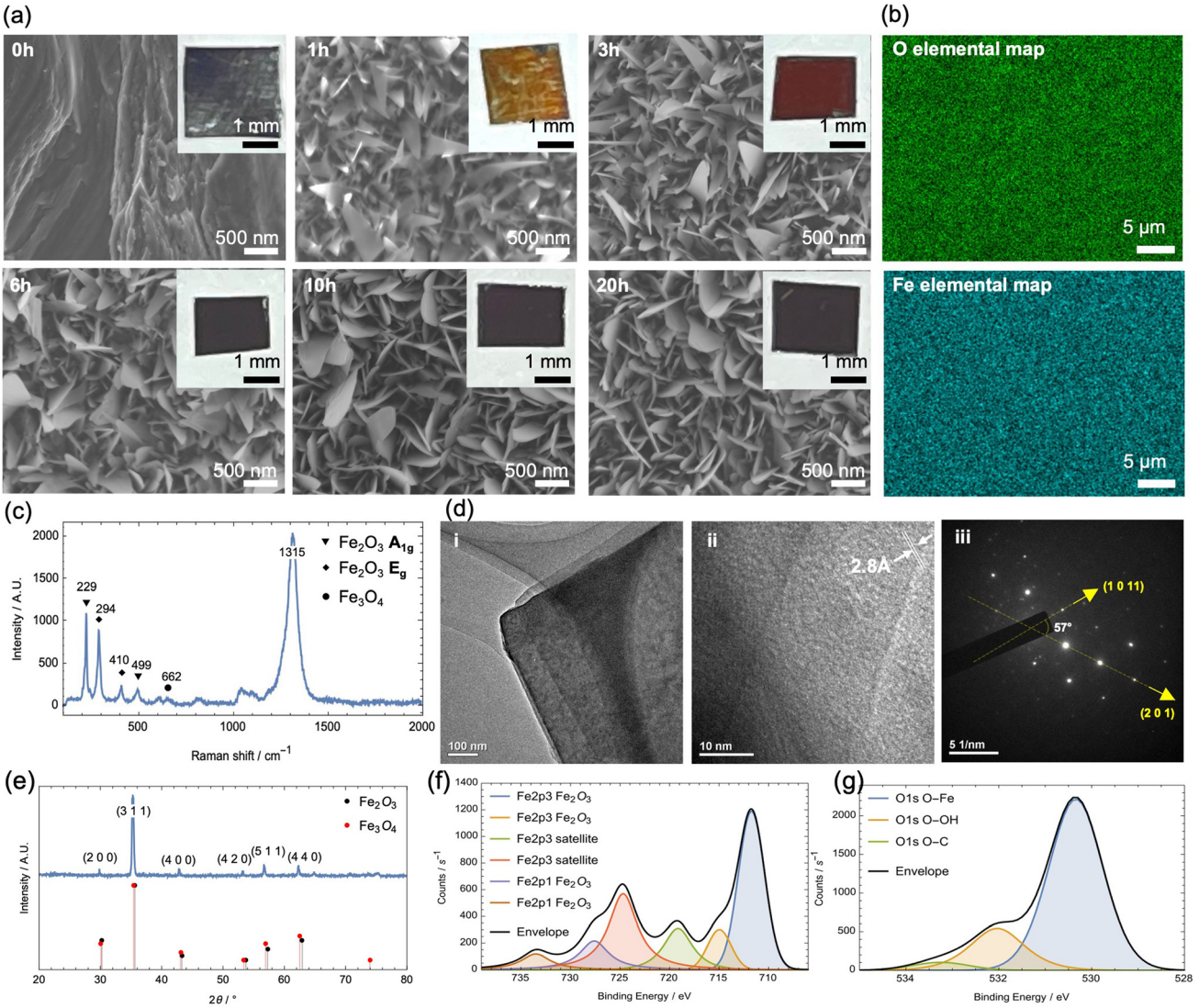

Fig. 1 (a) SEM images of the iron oxide nanoflakes formed after 0, 1, 3, 6, 10 and 20 hours of growth, with the corresponding optical images shown in the inset. (b) EDX elemental map of O and Fe elements, (c) Raman spectrum, (d) (i) TEM image, (ii) high-resolution TEM (HRTEM) image, (iii) SAED pattern, (e) XRD results and (f and g) XPS spectra showing the (f) Fe 2p and (g) O 1s scans of the iron oxide nanoflakes after 20 hours of growth.

shown as insets. Before heating, the pristine iron foil has a smooth and silvery appearance. Under SEM, it appears roughened (which is due to the sanding) but is not jagged. Referring to the inset for 1 hour of heating, a layer with the characteristic reddish-brown colouration of Fe_2O_3 can already be seen on the surface of the sample. The coverage density of this layer increases as the heating duration increases, causing the samples to appear darker visually. Under SEM, thin jagged nanoflakes are formed at shorter heating durations and they gradually become smoother, rounder and more uniform as the heating duration increases, causing the samples to appear darker visually. Under SEM, thin jagged nanoflakes are formed at shorter heating durations and they gradually become smoother, rounder and more uniform as the heating duration increases from 1 to 20 hours. Since they produced the most uniform nanoflakes, 20 hours of heat treatment was chosen for further investigation.

Elemental analysis was conducted on the nanoflake sample heated for 20 hours. The EDX elemental map reveals a uniform distribution of iron and oxygen elements across the samples (Fig. 1(b)). The result highlights the uniformity achieved through the simple hotplate-assisted synthesis process. Complementing the EDX analysis is the Raman spectrum of the sample, as shown in Fig. 1(c). The Raman spectrum of the sample is well matched to that of Fe_2O_3 and shows the characteristic peaks of Fe_2O_3 at 229 cm^{-1}, 294 cm^{-1}, 410 cm^{-1}, 499 cm^{-1}, 609 cm^{-1} and 1315 cm^{-1},[14] where the peaks at 229 cm^{-1} and 499 cm^{-1} correspond to the A_{1g} vibrational mode and the peaks at 294 cm^{-1}, 410 cm^{-1} and 609 cm^{-1} correspond to the E_g vibrational mode.[15] The 1315 cm^{-1} peak is due to a second-order scattering process and is specific for the two-phonon or two-magnon scattering process in Fe_2O_3.[16] There is also a peak at 662 cm^{-1} not tra-

ditionally associated with Fe_2O_3. This peak is close to that of magnetite (Fe_3O_4)'s main Raman peak and may be attributed to incomplete oxidation.[17,18]

The crystallinity of the synthesized nanoflake sample was examined through TEM and XRD analyses (Fig. 1(d and e)). Under lower magnification, as shown in Fig. 1(d(i)), it can be seen that the nanoflakes have sharp and well-defined edges. The high-resolution TEM (HRTEM) image of the region shown in Fig. 1(d(ii)) had a measured lattice spacing of 2.83 Å, corresponding to the hexagonal primitive Fe_2O_3 (113) plane (JCPDS PDF #40-1139). The bright, distinct spots arranged in a periodic manner obtained in the selected area electron diffraction (SAED) pattern (Fig. 1(d(iii))) indicate good crystallinity with single orientation within a single nanoflake. By analysing the *d*-spacing and angle between the planes, the SAED pattern was matched to the (1 0 11) and (2 0 1) planes of a hexagonal primitive Fe_2O_3 crystal structure.

The XRD results of the synthesised nanoflakes are matched to those of cubic Fe_3O_4 (JCDPS PDF#19-0629) and cubic Fe_2O_3 (JCDPS PDF#39-1346), and the corresponding Miller indices have been labelled on the respective peaks. The sample had a calculated crystallographic index (CI) of 31.7%. This indicates a mixture of Fe_3O_4 and Fe_2O_3, in agreement with the results of the other characterisation studies conducted.

Fe 2p and O 1s XPS spectra of the sample are presented in Fig. 1(f) and (g), respectively. As expected, signals at 712 eV, 715 eV, 727.5 eV, and 733.5 eV attributed to the bonding electrons of iron in Fe_2O_3 are observed, as well as a strong peak at 530.3 eV due to the O 1s electrons involved in O–Fe bonding is observed. There are also much weaker peaks from the O–OH and O–C bonds, which are likely attributed to water and carbon dioxide adsorbed onto the sample's surface.

3.2 Laser-initiated photo-reduction of silver on iron oxide nanoflakes

A focused laser beam (FLB) induces the formation of the silver–iron oxide nanocomposite *via* photothermal reduction of silver nitrate solution in the presence of an iron oxide substrate. A schematic of the laser set-up is shown in Fig. 2(a). By varying the laser's intensity and patterning speed as it interacts with the sample, the degree of photothermal reduction of silver nitrate solution in the presence of iron oxide can be tuned. This, in turn, changes the final chemical and physical properties of the formed silver–iron oxide nanocomposite.

The FLB was used to pattern 30 μm by 30 μm squares onto the sample with a raster motion, after which the lasered structures were observed under FM. Fig. 2(b) shows a typical optical image of the pristine sample. Upon viewing under bright-field excitation, the sample appears uniform and dark. However, it emits a dim red fluorescence under yellow excitation. An example of the lasered square is shown in Fig. 2(c). The formation of uniformly distributed bright blue specks within the lasered square region can be seen under bright field excitation, and these bright blue specks correspond to the points with bright red fluorescence under yellow excitation. To demonstrate how this deposition process has achieved site-selectivity in the formation of the silver-containing nanocomposite, a micro-pattern spelling out the words "NUS 120" was created and is shown in Fig. 2(d). Comparing the spectra obtained from the pristine and the lasered samples under yellow excitation (Fig. 2(e)), a significant 10.7 times increase in the fluorescence intensity is observed from the lasered sample. This strongly suggests that non-destructive optical characterisation can be a viable means to determine the successful formation of the silver–iron oxide composite.

3.3 Optimal lasering parameters

To determine the optimal parameter for the uniform synthesis of the silver–iron oxide nanocomposite across the lasered region, laser power densities of 3.82×10^9, 4.46×10^9 and 5.09×10^9 mW cm^{-2} and lasering speeds of 100, 150 and 200 μm s^{-1} were systematically varied (Fig. 2(f)). Since the incorporation of silver increased the observed red fluorescence, this would be indicative of more uniform and controlled formation of silver–iron oxide nanocomposites. Hence, fluorescence analysis was used to find the set of parameters that would yield the product with the brightest and most uniform fluorescence.

Through the optimisation process, a few important trends are noted. On one hand, at a lower laser power density (Fig. 2(f) A, D and G), there is little visible fluorescence. This is likely due to the low rate of photon incidence, which limits the formation of iron and oxygen ions. The formation of these ions is crucial in facilitating the synthesis of the silver–iron oxide nanocomposite. A more detailed discussion on the formation mechanism of this composite is presented in the subsequent section.

On the other hand, a higher laser power density (Fig. 2(f) C, F and I) also resulted in a significant decrease in fluorescence. Unlike the phenomenon observed at a lower laser power density, the lack of fluorescence at higher laser powers could be due to substantial ablation of the iron oxide nanoflake layer, leading to the exposure of the underlying Fe foil. This hypothesis is supported by the EDX elemental mapping (Fig. 3(d and e)), which demonstrated a marked reduction in the quantity of both Fe and O in the lasered region compared to the surrounding non-lasered region. This indicates that the underlying nanoflake substrate is ablated during the laser modification. Since the iron oxide nanoflakes are necessary for the formation of the fluorescent product, this causes the brightness to decrease at high powers. Finally, the uniformity of the fluorescence increases notably when the patterning speed increases, leading to an overall higher intensity. Similarly to the case with higher lasering power, at slower interaction speeds, there could be more significant ablation of the iron oxide nanoflake layer.

Quantification of the fluorescence observed under yellow excitation was achieved by analysing the area under the spectra obtained from individual squares (Fig. 2(g)). A laser power density of 4.46×10^9 mW cm^{-2} and a patterning speed of 200 μm s^{-1} (Fig. 2(f) H) were chosen for detailed characterisation as they yielded the brightest and most uniform fluorescence, indicated by the highest fluorescence peak (Fig. 2(g)). The systematic study thus provided a means to

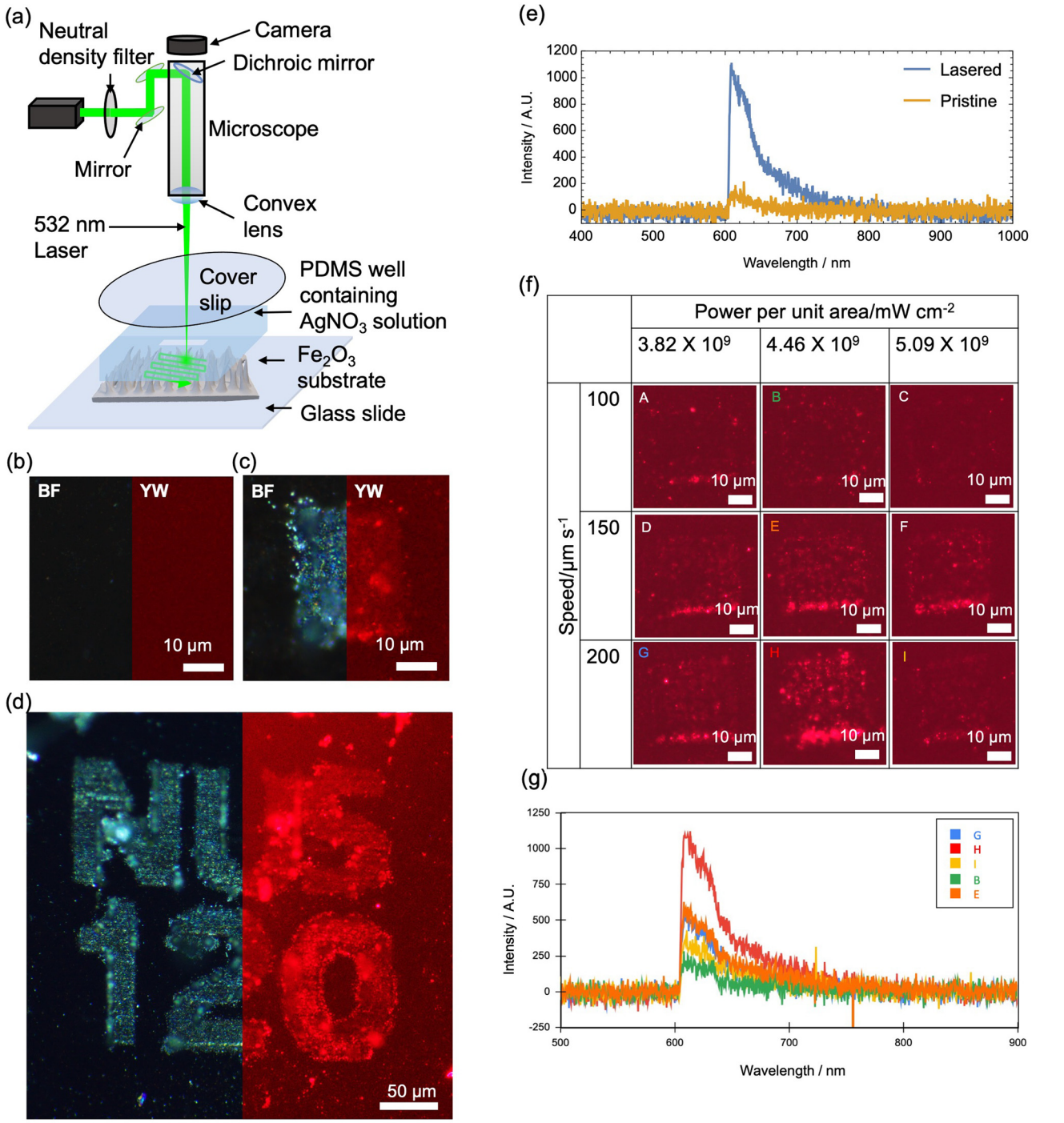

Fig. 2 (a) Schematic of the focused laser beam set-up. (b) Pristine sample and (c) lasered micro square under bright field (left) and yellow excitation (right). (d) Micro pattern of words "NUS 120" observed under bright field (left) and yellow excitation (right). (e) FM spectra of the pristine and lasered samples under yellow excitation. (f) FM images of lasered squares with various lasering parameters and (g) the corresponding fluorescence spectra from (f).

identify the optimal parameter for the formation of the silver–iron oxide nanocomposite. Thereafter, samples created under the optimal conditions will be labelled as "lasered" and detailed characterisation studies with comparisons to pristine samples will be carried out.

Under SEM, secondary electron imaging (SEI) was first used to observe the surface morphology of the silver–iron oxide nanocomposites. Fig. 3(a) shows the lasered square exhibiting a distinct morphological difference compared to the surrounding pristine region. The higher magnification image in

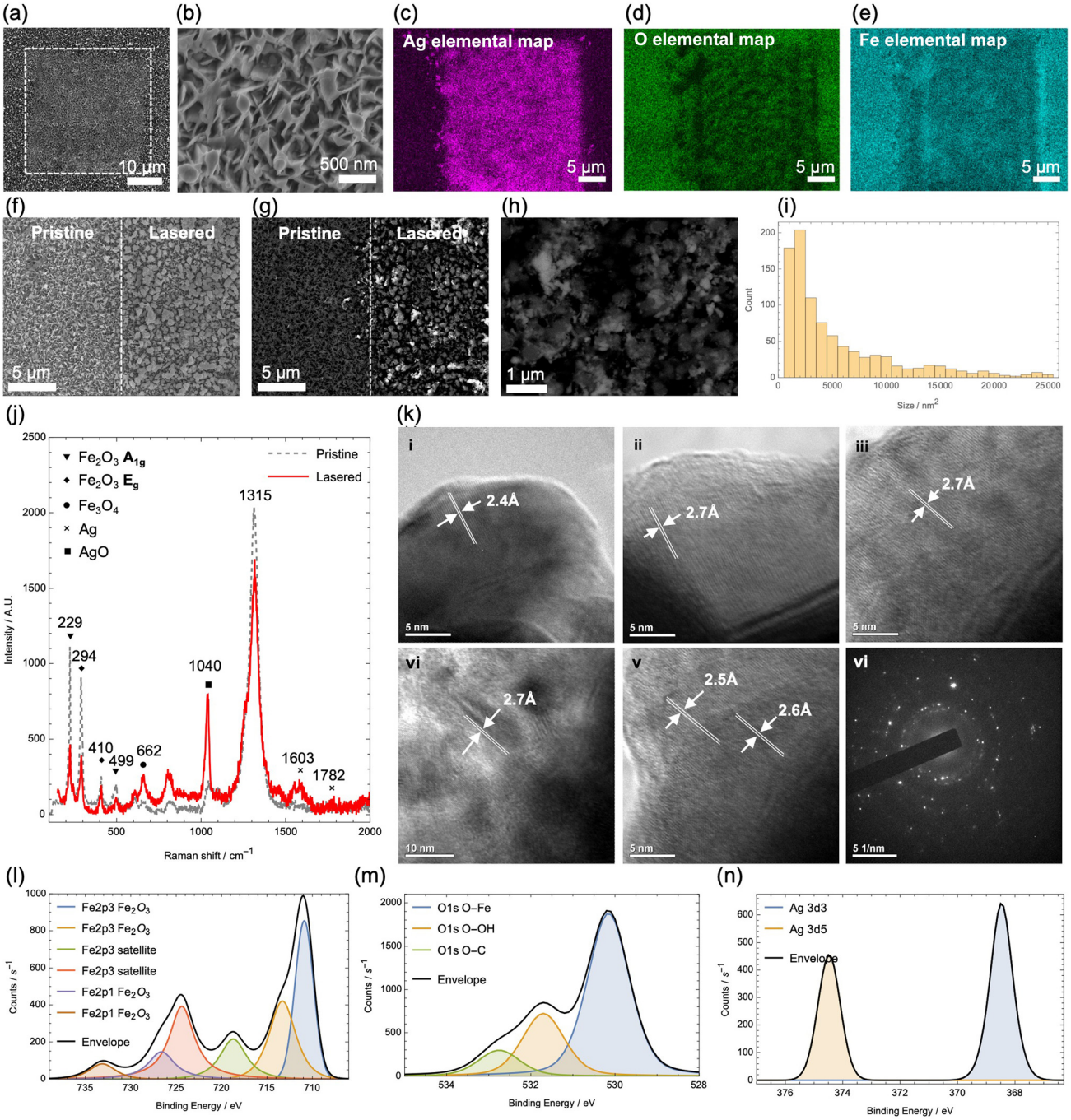

Fig. 3 Lasered square under SEM with secondary electron imaging (SEI) taken at (a) lower and (b) higher magnification. EDX element map of (c) Ag, (d) O, and (e) Fe from the lasered square. (f) Pristine (left) and lasered (right) regions under SEM with secondary electron imaging and (g) with backscatter electron (BSE) imaging of the same region. (h) Lasered region under SEM with BSE imaging at higher magnification. (i) Histogram showing size distribution of silver nanoparticle deposits. (j) Raman spectrum of the lasered region. (k) (i–v) HRTEM images of the silver–iron oxide nanocomposite and (vi) SAED pattern of the nanocomposite. (l–n) XPS spectra of (l) Fe 2p, (m) O 1s, and (n) Ag 3d scans.

Fig. 3(b) shows the formation of spherical protrusions on the nanoflake tips in the lasered sample. Elemental mapping of Ag, O and Fe from the EDX analysis performed on the lasered square is presented in Fig. 3(c–e). Ag is distributed only in the lasered region, while there is a reduction in the density of Fe and O in the lasered region.

To conduct a statistical study on the size and distribution of the formed Ag nanoparticle protrusions, backscattered electron (BSE) imaging was conducted on the lasered sample. Fig. 3(f) and (g) show the same region observed using secondary (f) and backscattered (g) electrons. Since Ag has a larger atomic mass than Fe_2O_3 and Fe_3O_4, the regions where Ag is

present appear brighter under BSE, as shown in Fig. 3(g). This allows them to be identified using a threshold filter. Image analysis was conducted using ImageJ,[19] and more details can be found in Fig. S2. 20 images taken under a higher magnification using BSE, such as the one in Fig. 3(h), were analysed and a histogram of the size distribution of the Ag nanoparticles was plotted and is shown in Fig. 3(i). The Ag nanoparticles follow a right-skewed distribution, with 80% of the particles falling below the size of 9000 nm^2. Using the same principle, the nanoparticle size distribution for 2 different speeds was also compared. The speed of 50 μm s^{-1} yielded smaller silver particles compared to that of 200 μm s^{-1}, demonstrating how the nanoparticle size can be tuned by varying lasering parameters. The histograms of the distributions are presented in Fig. S3.

Raman analysis (Fig. 3(j)) of the lasered sample shows a strong peak at 1040 cm^{-1}, which is attributed to Ag,[20] and the peaks at 1603 cm^{-1} and 1782 cm^{-1} are attributed to AgO (Fig. 3(k)),[21] thus verifying the successful formation of silver and silver oxide on the iron oxide nanoflakes.

Subsequently, the lasered sample was imaged under HRTEM and the images taken are presented in Fig. 3(k). Under lower magnification (Fig. 3(k(i–iii))), the silver nanocomposite structures appear round, with a range of lattice spacings corresponding to the (004) plane of Ag (2.5 Å, JCPDS PDF#: 41-1402) and the (200) plane of Ag_2O (2.6 Å, JCPDS PDF#: 41-1104). The SAED pattern obtained from the lasered sample is presented in Fig. 3(k(vi)). The bright spots arranged in a ring pattern indicate a polycrystalline structure with differing crystal orientations.

The XPS spectra of the lasered sample are presented in Fig. 3(l–n). Peaks attributed to 3d3 and 3d5 electrons in elemental silver were obtained. Remarkably, there were no peaks attributed to the obtained Ag–O bonding electrons. After laser patterning, there was a decrease in the percentage of O 1s electrons involved in O–Fe bonding from 38.2 to 16.4 and a decrease in the percentage of Fe 2p electrons in Fe_2O_3 from 16.0 to 13.2, indicating that bonds were broken within the iron oxide substrate.

3.4 Proposed mechanism

Based on the characterisation conducted, the following mechanism for the formation and fluorescence phenomenon of the silver-oxide nanocomposite structure is proposed.

The Fe_2O_3/Fe_3O_4 in the nanoflakes absorbs energy from the 532 nm laser beam, which falls within their absorption spectra,[22] and converts it to heat. This photothermal process, as described in eqn (1) and (2), results in partial melting of the tips of the nanoflakes, forming O^{2-}, Fe^{2+} and Fe^{3+} ions in solution:

$$Fe_2O_3(s) \rightarrow 2Fe^{3+}(aq) + 3O^{2-}(aq) \quad (1)$$

$$Fe_3O_4(s) \rightarrow 2Fe^{3+}(aq) + Fe^{2+}(aq) + 4O^{2-}(aq) \quad (2)$$

Within the immediate surrounding of the nanoflakes, there is a high concentration of O^{2-} ions, which causes silver oxides to precipitate from the solution and form nanoparticles that are anchored onto the Fe_2O_3 nanoflakes:

$$2Ag^{+}(aq) + O^{2-}(aq) \rightarrow 2AgO(s) \quad (3)$$

$$4Ag^{+}(aq) + O^{2-}(aq) \rightarrow 2Ag_2O(s) \quad (4)$$

The silver oxides are sensitive to light and the surface layer will readily decompose into Ag:

$$2AgO(s) \rightarrow 2Ag(s) + O_2(g) \quad (5)$$

$$2Ag_2O(s) \rightarrow 4Ag(s) + O_2(g) \quad (6)$$

This process is summarised in Fig. 4(a). A further observation that supports the proposed mechanism is the consistent formation of air bubbles, as shown in Fig. 4(b), after a prolonged period of lasering. The diffused (unfocused) laser spot seen in time t = 2 s–10 s is due to the refraction of the laser beam as it passes through an air bubble and was observed after 150 s of laser patterning. A video of the bubble formation process can be found in Video S1. The possibility that the air bubbles are merely due to the solution boiling is ruled out by repeating the laser patterning process in deionised water, which did not produce such air bubbles even after the protracted periods of laser treatment. A video of this can be found in Video S2. This formation mechanism also explains the presence of silver oxides detected in Raman spectroscopy but not in XPS, as Raman excitation has a deeper probe depth (100 μm) than XPS (<100 Å), and the photodecomposition in eqn (4) and (5) will only affect the surface layer of silver oxides.

We also do not rule out the possible contribution of direct photoreduction of the Ag^{+} ions. Since the photon energy of the laser (2.3 eV) exceeds the band gaps of Fe_2O_3 (1.9–2.2 eV (ref. 23)) and Fe_3O_4 (2.1 eV (ref. 24)), photogeneration of electrons *via* this means is also possible.[25,26] This process can also produce oxygen bubbles by serving as a sacrificial reaction for water oxidation by the generated holes.[27]

The fluorescence mechanism of the nanocomposite can be explained *via* the nanoflakes' inherent fluorescence and the nano silver deposition's enhancement effect.

Fig. 4(c) shows the PL spectra of the lasered and pristine samples under 532 nm excitation. The samples exhibited the strongest emission peak centred at 691 nm. However, the intensity is greatly strengthened in the lasered sample, which supports the suggestion that incorporating Ag mainly enhances the fluorescence already associated with the iron oxide nanoflakes. According to Shi *et al.* (2015)[28] and Sadat *et al.* (2014),[29] an emission at around 690 nm is associated with the recombination of trapped electrons from the octahedral site to O(2p) in crystalline Fe_2O_3 and Fe_3O_4, which have similar electronic band structures and both go through this transition[30] (Fig. 4(d)).

From the analysis of the Raman spectrum in Fig. 3, the peak associated with Fe_3O_4 at 662 cm^{-1} increases in intensity relative to other peaks after the incorporation of silver. The enhanced Raman scattering points to the localised surface

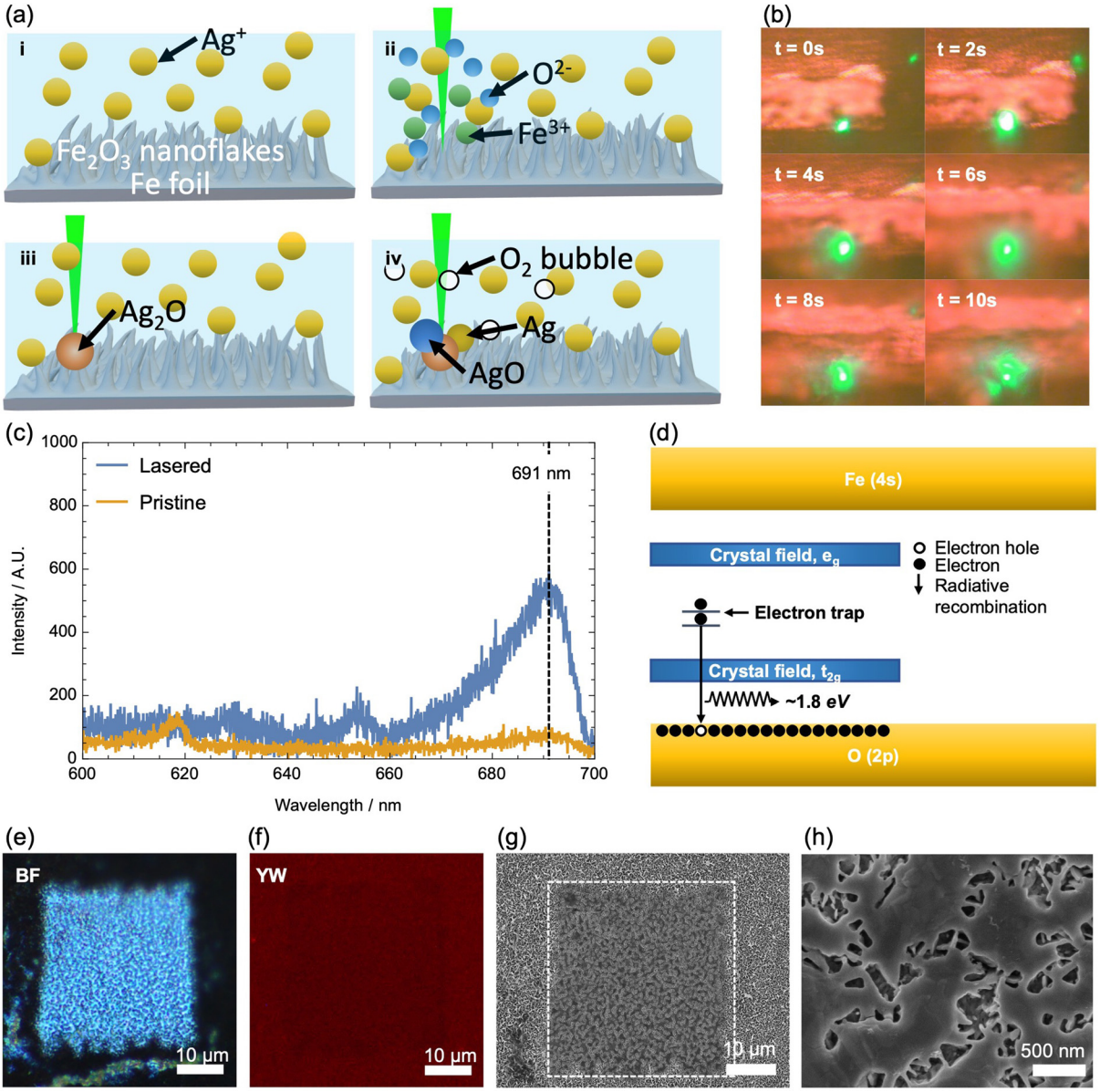

Fig. 4 (a) Labelled 3D schematic of the proposed mechanism for the formation of the silver–iron oxide nanocomposite. (b) Screengrabs (within 10 seconds) of laser patterning of the Fe_2O_3/Fe_3O_4 nanoflakes in $AgNO_3$ (aq), where the formation of an air bubble is observed. (c) PL spectra of the lasered and pristine squares. (d) Energy level diagram showing the proposed electronic transition responsible for fluorescence emission. (e) FM images of a micro-square lasered in de-ionised water observed under bright field and (f) yellow excitation. (g and h) SEM images of micro-square lasered in de-ionised water taken at lower and higher magnifications. The dotted square in (g) highlights the location of the laser-patterned region. (h) Higher magnification SEM image taken within the laser-patterned region.

plasmon resonance of silver on Fe_3O_4, which produces intense electric fields in the near field. Thus, while both Fe_2O_3 and Fe_3O_4 are responsible for the inherent red fluorescence of the iron oxide nanoflakes, Fe_3O_4 is important for the laser-initiated enhancement effect due to its interaction with silver.

The proposed mechanism is verified by repeating a similar laser treatment of the iron oxide nanoflakes in de-ionised water. The results are reported in Fig. 4(e–h). As shown in Fig. 4(e and f), without the presence of Ag, there is no enhancement of the underlying red fluorescence. In fact, notably, the lasered sample region appears noticeably dimmer than the surrounding regions. Observing the same lasered square under SEM (Fig. 4(g) and (h)), it can be seen that lasering in de-ionised water had caused the Fe_2O_3/Fe_3O_4 substrate's flake-like surface to melt and flatten into a smoothened one. This would have increased the characteristic length of the nanoflakes greatly and may have caused their innate fluorescence, which have been reported to be size-dependent,[31] to decrease or disappear.

4 Applications

During characterisation, it was discovered that after conducting EDX analysis on a laser-patterned square, the area treated with electrons shows an increase in fluorescence intensity, while the neighbouring regions do not.

To prove that this effect is in fact due to electron irradiation, a large lasered sample was prepared and a copper (Cu) TEM grid was placed over the lasered region (Fig. 5(a)). The grid serves as a mask that blocks electrons from interacting with the regions of the lasered sample below the grid lines, leaving only regions in the grid gaps exposed to electron irradiation. The EDX elemental map shows that the grid is mapped to the element Cu, while the exposed region only indicates the presence of Ag and Fe (Fig. 5(b and c)). After this preparation, the sample was placed under the SEM's high-energy electron beam (Fig. 5(d)). In doing so, one would expect the electron-bombarded silver–iron oxide nanocomposite located in the grid gaps to emit stronger fluorescence under yellow excitation. In other words, removing the TEM mask will allow an "invisible" mask to be observable based on the fluorescence contrast.

Indeed, before the electron treatment, the laser-patterned region exhibits a uniform distribution of bright blue specks under bright field excitation and uniform red fluorescence under yellow wavelength excitation (Fig. 5(e)). After electron treatment, no grid pattern is observed under BF imaging. However, the intensity of the red fluorescence under yellow excitation was found to increase only in the exposed areas of the sample. As a result, an invisible mask highlighting a "crosshatch" pattern comprising regions with various intensities of red fluorescence is formed (Fig. 5(f)).

This effect was quantitatively understood by repeating the electron bombardment process with different electron dosages and observing the fluorescence changes. Electron dosage is defined as:

$$\text{Dose} = It/A \tag{7}$$

where I is the current, t is the duration of irradiation, and A is the dosed area.

1 dose is defined as 2.55×10^6 cm^2 and was achieved through directing a high-energy beam of 15 keV and a current of 15 μA on a 30.0 μm × 53.3 μm area for 6.36 min. The fluorescence intensity is quantified by integrating the area under the fluorescence spectrum graph. FM images of a set of squares before and after varying dosages of electrons are shown in Fig. 6(a), while the percentage change in the fluorescence intensity against electron dosage is plotted in Fig. 6(b). The percentage increase in fluorescence brightness shows an increasing trend with electron dosage. The experiment was repeated twice to ensure repeatability, with the results showing a similar increasing trend. These results are presented in Fig. S4. These spatial resolution and detection range metrics are comparable to popular contemporary detec-

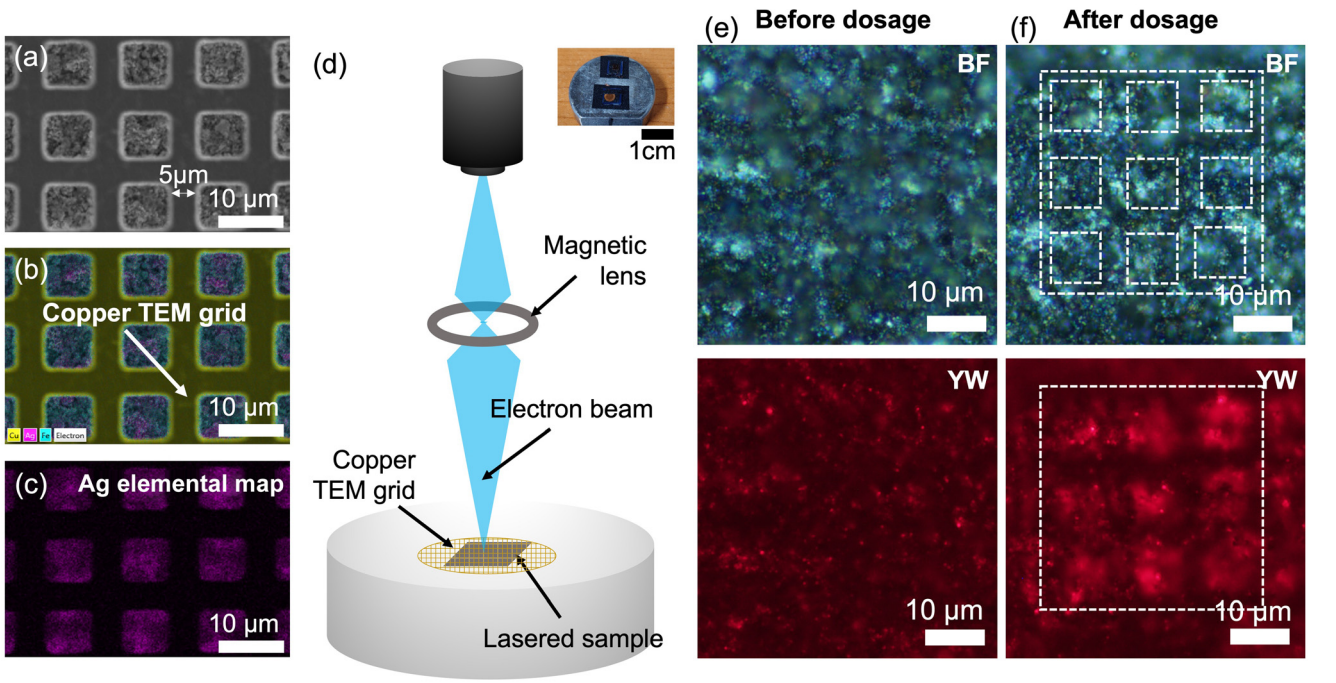

Fig. 5 (a) SEM image of the copper TEM grid mask being placed over a large area of the silver–iron oxide nanocomposite. (b) EDX element map of Ag, Cu and Fe overlaid in the SEM image of the copper TEM grid placed over the sample. (c) Ag element map highlighting the presence of Ag element only within the grid's exposed region. (d) A 3D schematic of the electron dosage set-up. Silver–iron oxide nanocomposite (e) before and (f) after electron dosage under BF (above) and yellow (below) excitation. The dotted lines in the inset of (f) serve a visual guide to highlight the original masked region.

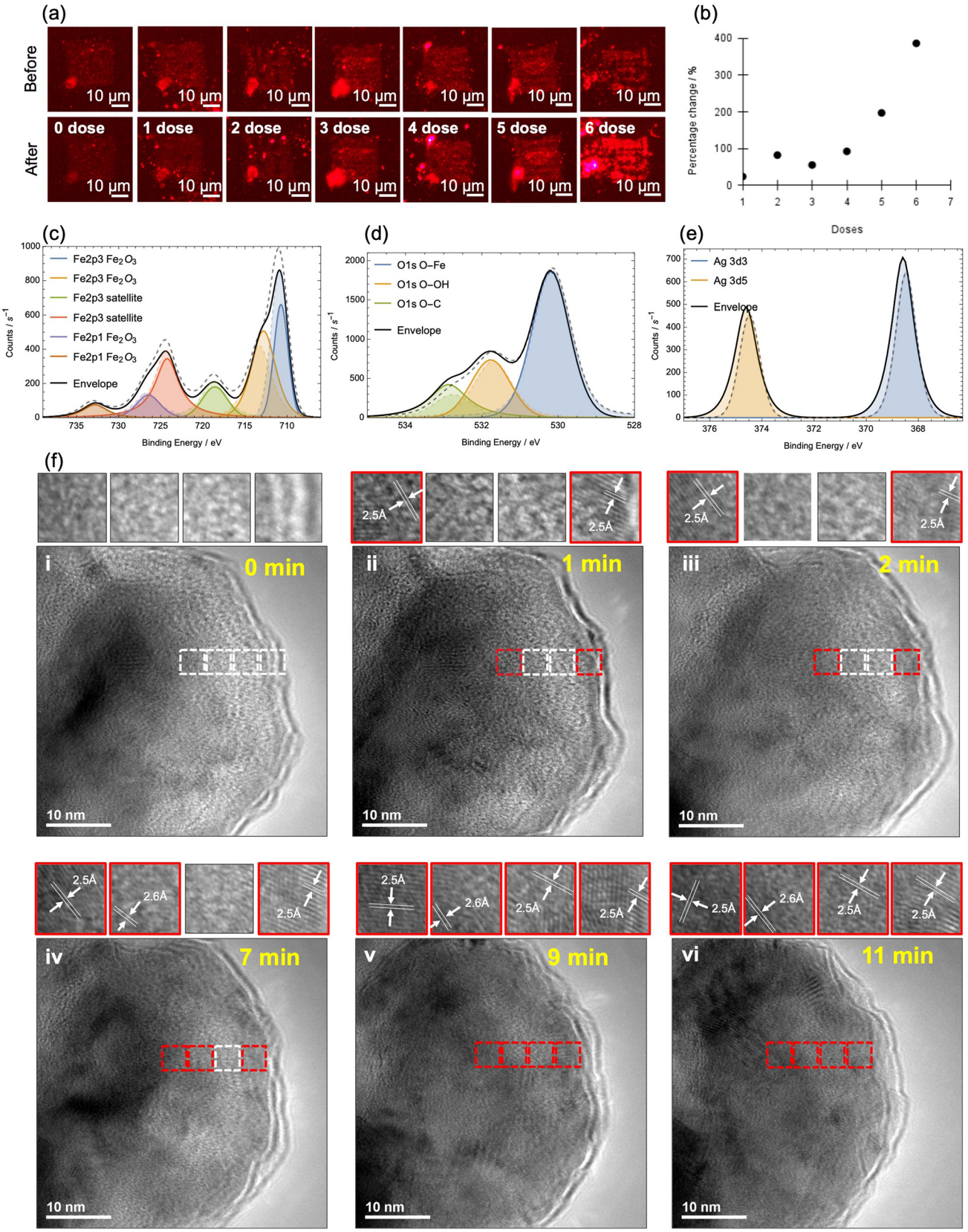

Fig. 6 (a) Lasered sample before (above) and after (below) electron bombardment. (b) Plot of the percentage change of fluorescence intensity against electron dosage. XPS spectra of the (c) Fe 2p, (d) O 1s, and (e) Ag 3ds scans of the electron-treated sample. The spectrum of the laser-treated but not electron-treated sample is also plotted on the same axes in dashed lines to aid in comparison. (f) HRTEM images of the same region of a lasered sample after (i) 0 min, (ii) 1 min, (iii) 2 min, (iv) 7 min, (v) 9 min, and (vi) 11 min of electron bombardment.

tors and a more detailed comparison table can be found in Table S1.

To achieve a fundamental understanding of the aforementioned phenomenon, XPS analyses were conducted on the electron-treated sample (Fig. 6(c–e)). The spectra of the lasered but not electron-treated sample were also plotted on the same axes in dashed lines to aid in comparison. It is determined that after electron bombardment, the Ag 3ds and 5ds peaks shifted to a higher binding energy. Since Ag in the metallic form is known to exhibit a higher binding energy relative to silver oxide,[32] such a shift could indicate the reduction of silver oxides into metallic silver taking place when the sample is treated with high-energy electrons. Note that it is not only just Ag but also Fe that shows reduction after electron bombardment. There is a rightward shift of the Fe 2p3 peaks after bombardment to a lower binding energy, which indicates the conversion of Fe^{3+} to Fe^{2+}.[33]

The process of electron-initiated transformation of silver oxide to silver is observed under TEM imaging. By capturing a series of TEM images of the same region over a period of time, *in situ* transformation of Ag_2O to Ag in the presence of electron bombardment is observed by capturing how the crystallinity of Ag_2O changes. The laser-patterned sample was transferred onto a TEM grid and multiple consecutive images were captured. The series of images taken is presented in Fig. 6(f), where the white/red dotted boxes are included as a visual guide to highlight the transformation of amorphous AgO (white dotted boxes) to crystalline Ag (red dotted boxes).

At 0 min (Fig. 6(f(i))), regions within the four white dotted boxes begin in an amorphous state. After 1 min (Fig. 6(f(ii))) and 2 min (Fig. 6(f(iii))) of electron bombardment, lattice structures with spacings corresponding to 2.5 Å are visible in the two outermost regions (highlighted by the red boxes). The spacing corresponds to the (004) plane of Ag (JCPDS PDF #41-1402). With 7 min of electron interactions (Fig. 6(f(iv))), the crystalline region extended from the inner region towards the outer region. The newly transformed region also has a lattice spacing of 2.5 Å. At 9 min (Fig. 6(f(v))), the region of interest has fully converted from an amorphous state to a crystalline state, with the entire region composed of an orderly lattice of crystalline Ag with a lattice spacing of 2.5 Å. The crystallinity remains stable even after an additional 2 min (Fig. 6(f(vi))) of electron bombardment. This suggests that the electron dose has led to the formation of Ag from the amorphous material, which is likely to be a mixture of Ag_nO compounds formed during laser patterning. As silver metal but not oxides of silver can enhance fluorescence *via* surface plasmon resonance, the conversion of the surface silver oxide nanostructures into silver readily explains the observed enhancement of the red fluorescence.

As expected from this mechanism, the enhanced fluorescence decays over time when stored under ambient conditions, as the silver generated from the reaction with bombarding electrons reacts readily with atmospheric oxygen to revert to silver(I) oxide. A visual comparison of the sample's decreasing fluorescence after 0 days, 9 days and 1.5 years, as well as their emission spectra under yellow light excitation, are included in Fig. S5.

5 Conclusions

In summary, this work presents an alternative way to synthesise silver–iron oxide composite nanostructures using a focused laser beam. Submerging the Fe_2O_3/Fe_3O_4 nanoflake substrate in a solution full of silver ions, while introducing a focused laser beam onto the sample, causes the Fe_2O_3/Fe_3O_4 nanoflakes to generate localised heat, which facilitates photothermal reduction of Ag ions at the specific site. This leads to the uniform and site-selective formation of a silver–iron oxide nanocomposite in the lasered region. Uniquely, bright red fluorescence from the composite is observed and attributed to the Ag nanostructure's enhancement of the Fe_2O_3/Fe_3O_4's intrinsic fluorescence through surface plasmon resonance effects. Such an optical phenomenon not only allows facile, direct visual determination of the formation and change in the oxidation state of the Ag nanostructure, but also enables the silver–iron oxide nanocomposite to function as an effective micro-beta particle detector with real-time optical feedback. Looking forward, the development of alternative synthesis processes is a viable path towards unravelling non-traditional applications of nanocomposites.

Author contributions

Yue Yin: writing – review and editing, writing – original draft, methodology, investigation, formal analysis, and data curation. Aseera Jannath: writing – original draft, methodology, investigation, and data curation. Zheng Zhang: methodology and investigation. Sharon Xiaodai Lim: writing – review and editing, writing – original draft, supervision, project administration, and conceptualisation. Chorng Haur Sow: writing – review and editing, writing – original draft, supervision, resources, project administration, and conceptualisation.

Conflicts of interest

There are no conflicts to declare.

Data availability

The data supporting this article have been included as part of the SI: time-dependent Raman spectra and XRD data for nanoflake growth; image processing pipeline for size distribution analyses; a histogram showing the particle size distribution at different lasering speeds; a plot of changes in fluorescence intensity with different amounts of electron dosage; fluorescence microscopy images under yellow excitation and spectra showing the stability of fluorescence; a table comparing electron detection capabilities with contemporary sensors;

a video of bubble formation during lasering in $AgNO_3$, and a video of no bubble formation during lasering in de-ionised water. See DOI: https://doi.org/10.1039/d5nr02284c.

Acknowledgements

The authors acknowledge the generous support from the Singapore MOE-ARC grant (A-8001494-00-00).

References

1 M. K. Hossain, A. Mishra, A. Tiwari, B. Pant, S. C. Dey, A. Tiwari, O. Saha, M. M. Rahaman, Y. R. Shukla, A. Tiwari and M. Ashaduzzaman, *SN Appl. Sci.*, 2023, **5**, 339.
2 M. A. Rabbi, M. B. Akter, B. M. Chaki, M. A. Latif, M. Al-Amin, M. Z. U. Rasel, S. Sharmin, M. Abdurrahim, M. H. K. Rubel and M. R. Habib, *New J. Chem.*, 2024, **48**, 5278–5288.
3 S. A, A. Thamer, R. K, P. A, R. V, M. K, A. Murad and M. P, *J. Photochem. Photobiol., B*, 2020, **207**, 111885.
4 S. Vijayaraghavan, A. Rajasekaran, A. N. Alodhayb, M. Muthuramamoorthy, M. Vimalan and K. Ganesh Kumar, *Mater. Sci. Eng., B*, 2025, **311**, 117801.
5 A. Mirzaei, K. Janghorban, B. Hashemi, A. Bonavita, M. Bonyani, S. G. Leonardi and G. Neri, *Nanomaterials*, 2015, **5**, 737–749.
6 S. Liu, Y. Chen and L. Dong, *Mater. Res. Express*, 2016, **3**, 075024.
7 V. T. Trang, L. T. Tam, V. N. Phan, N. Van Quy, T. Q. Huy and A.-T. Le, *J. Electron. Mater.*, 2017, **46**, 3323–3332.
8 K. Nasiri, *Nanomed. Res. J.*, 2023, **8**, 283–289.
9 F. A. M. Al-Zahrani, S. S. Salem, H. A. Al-Ghamdi, L. M. Nhari, L. Lin and R. M. El-Shishtawy, *Bioengineering*, 2022, **9**, 452.
10 F. A. M. Al-Zahrani and R. M. El-Shishtawy, *Green Process. Synth.*, 2024, **13**, 20230218.
11 N. S. Mohan, R. Gokulkumar, J. Shankar, R. Sridharan, B. Logesh, R. Sasikumar, K. Vallarasu and V. Vijayalakshmi, *Results Chem.*, 2022, **4**, 100626.
12 Z. Chai, A. Childress and A. A. Busnaina, *ACS Nano*, 2022, **16**, 17641–17686.
13 T. Yu, Y. Zhu, X. Xu, K.-S. Yeong, Z. Shen, P. Chen, C.-T. Lim, J. T.-L. Thong and C.-H. Sow, *Small*, 2006, **2**, 80–84.
14 H. Mansour, H. Letifi, R. Bargougui, S. De Almeida-Didry, B. Negulescu, C. Autret-Lambert, A. Gadri and S. Ammar, *Appl. Phys. A*, 2017, **123**, 787.
15 P. Kumar, H. No-Lee and R. Kumar, *J. Mater. Sci.: Mater. Electron.*, 2014, **25**, 4553–4561.
16 M. Lübbe, A. M. Gigler, R. W. Stark and W. Moritz, *Surf. Sci.*, 2010, **604**, 679–685.
17 D. Bersani, P. P. Lottici and A. Montenero, *J. Raman Spectrosc.*, 1999, **30**, 355–360.
18 A. M. Jubb and H. C. Allen, *ACS Appl. Mater. Interfaces*, 2010, **2**, 2804–2812.
19 C. A. Schneider, W. S. Rasband and K. W. Eliceiri, *Nat. Methods*, 2012, **9**, 671–675.
20 U. Agarwal, R. Reiner and J. Beecher, 15th International Symposium on Wood, Fiber, and Pulping Chemistry, 2009.
21 R. Nagiri, PhD thesis, IIT Madras, 2011.
22 M. Jeyavenkatesh, J. Arunodaya and T. Sahoo, *IOP Conf. Ser.:Mater. Sci. Eng.*, 2022, **1219**, 012043.
23 O. Seo, A. Tayal, J. Kim, C. Song, Y. Chen, S. Hiroi, Y. Katsuya, T. Ina, O. Sakata, Y. Ikeya, S. Takano, A. Matsuda and M. Yoshimoto, *Sci. Rep.*, 2019, **9**, 4304.
24 S. Delice, M. Isik and N. M. Gasanly, *Chem. Phys. Lett.*, 2024, **840**, 141139.
25 P. Luan, M. Xie, D. Liu, X. Fu and L. Jing, *Sci. Rep.*, 2014, **4**, 6180.
26 B. S. Zou and V. Volkov, *J. Phys. Chem. Solids*, 2000, **61**, 757–764.
27 T. H. Jeon, D. Monllor-Satoca, G. Moon, W. Kim, H. Kim, D. W. Bahnemann, H. Park and W. Choi, *Nat. Commun.*, 2020, **11**, 967.
28 D. Shi, M. E. Sadat, A. W. Dunn and D. B. Mast, *Nanoscale*, 2015, **7**, 8209–8232.
29 M. Sadat, M. Kaveh, A. Dunn, H. Wagner, R. Ewing, J. Zhang, H. Xu, G. Pauletti, D. Mast and D. Shi, *Appl. Phys. Lett.*, 2014, **105**, 091903.
30 C. Boxall, G. Kelsall and Z. Zhang, *J. Chem. Soc., Faraday Trans.*, 1996, **92**, 791–802.
31 Y. Zhang, W. Liu, C. Wu, T. Gong, J. Wei, M. Ma, K. Wang, M. Zhong and D. Wu, *Mater. Res. Bull.*, 2008, **43**, 3490–3494.
32 A. M. Ferraria, A. P. Carapeto and A. M. Botelho do Rego, *Vacuum*, 2012, **86**, 1988–1991.
33 T. Yamashita and P. Hayes, *Appl. Surf. Sci.*, 2008, **254**, 2441–2449.

